Pergamon

Int. J. Heat Mass Transfer. Vol. 37, No. 14, pp. 2077–2087, 1994

0017–9310/94 $7.00+0.00

0017–9310(94)E0041–R

Enhancement of heat transfer in square helical ducts

R. M. EASON, Y. BAYAZITOGLU† and A. MEADE

Department of Mechanical Engineering and Material Science, Rice University, Houston, TX 77251-1892, U.S.A.

(*Received* 1 *September* 1993 *and in final form* 24 *January* 1994)

Abstract—A three-dimensional numerical investigation of steady laminar flow and heat transfer is undertaken to determine the developing as well as fully developed temperature fields. Physical interpretation is given for the enhancement of the heat transfer coefficient at the thermal entrance region and the overall increase in heat transfer in helical ducts compared to straight ducts. The variation of peripherally averaged Nusselt number is studied for the constant wall temperature boundary condition. Detailed analysis is given for the peripheral variation of Nusselt number and the temperature field at different cross-sectional planes. The effect of the Prandtl number on the temperature field is also studied. The problem is solved using a segregated solution approach which reduces the total computer memory requirements.

INTRODUCTION

THE PROBLEM of flow through helical pipes and heat transfer is of importance in the fields of turbo-machinery, different process equipment and heat exchangers. The flow in curved ducts and helical pipes has been extensively investigated for Newtonian fluids, but the analysis does not exist for heat transfer in helical pipes of square cross-section and small aspect ratios. The solution of flow in helical pipes is complicated due to the effect of centrifugal forces which causes a secondary flow.

Using the friction factor measurement, White [1] reported the flow through a helicoidal pipe remains laminar at a larger Reynolds number than for the same straight pipe. The study by Largaespada *et al.* [2] showed from the friction factor measurements that the flow remains laminar until $Re \approx 8000$ which is much higher than the critical Reynolds number for the straight pipe. Hsu and Patankar [3] present the average Nusselt number data for different Prandtl numbers and Dean numbers for laminar non-Newtonian flow in curved tubes. Mori *et al.* [4] performed boundary layer type analysis of the fully developed laminar flow in a curved duct of square cross-section with uniform wall temperature. Analysis by Kumar [5] confirms the existence of dual solutions for a certain range of Dean number for fully developed flow of power law fluids in helical ducts. Joseph *et al.* [6] studied the laminar flow in helically coiled tubes of square cross-section. Cheng and Akiyama [7] studied the fully developed flow through curved rectangular channels. Numerical studies by Ghia and Sokhey [8] also indicate the presence of Dean's instability but at a Dean number of 143. Other numerical studies on the asymptotic flow through curved ducts show that the secondary flow breakdown takes place around a Dean number of 125, and the four-vortex structure exists even at a Dean number as high as 900.

A three-dimensional straight duct flow with a square cross-section is modeled to confirm the accuracy of the numerical procedure. The flow and heat transfer is analysed for a helical pipe of aspect ratio 6 for a constant wall temperature boundary condition. The Navier–Stokes equations were solved using the program FIDAP [9] which utilizes the Galerkin finite element method. The local heat transfer coefficient results show agreement with that of Chandrupatla and Sashi [10]. The local variation of Nusselt number along the length and along the perimeter is analysed. The flow through the helical pipe is analysed for a Dean number range of 20–1300 for a helicoidal duct of aspect ratio (R/a) 13 and pitch $1.68D$. The appearance and disappearance of additional counter rotating vortices are discussed in this section. This gives the design parameters at the entrance length for a square helical pipe of this aspect ratio and pitch. The effect of pitch on the local variation of Nusselt number along the periphery is also discussed here. In subsequent sections flow and heat transfer in a helical duct of aspect ratio $R/a = 3$ and pitch $1.68D$ is modeled. The flow and heat transfer is analysed for Reynolds number of 500 and 750 and for Prandtl numbers 0.7, 3.0 and 7.01. The axial velocity profiles were compared for the same axial length for the straight duct, and the three helical ducts. In all the cases the pitch of the helix is kept constant at $1.68D$. For the helical ducts of aspect ratio 3 and 6, values were obtained for two set of Reynolds number, 500 and 750. For the helical duct of aspect ratio 13, the heat transfer characteristics are analysed for three sets of Reynolds numbers, 750, 1250 and 1750.

† Author to whom correspondence should be addressed.

NOMENCLATURE

a half the width of one edge of the square cross-section of duct
A_c flow cross-sectional area [m^2]
b pitch of the helix
C_p specific heat
D width of one edge of the cross-section of the duct, $2a$
D_h hydraulic diameter of the duct, $4A_c/P$
f_u u component of the forcing vector, **F**
f_v v component of the forcing vector, **F**
f_w w component of the forcing vector, **F**
F forcing vector
k_f thermal conductivity of fluid
L length of the straight duct
$Nu_{x,bc}$ peripheral average axially local Nusselt number for the thermal entrance region for the specified thermal boundary condition, based on T_0
$Nu_{x^*,bc}$ peripheral average axially local Nusselt number for the thermal entrance region, based on T_m
P wetted perimeter of the duct [m]
p nondimensional pressure
R centerline radius of curvature of helix
T temperature
ΔT temperature difference
T_m bulk mean temperature
T_0 inlet temperature
T^* nondimensional temperature
U_0, V_0, W_0 inlet x, y and z components of velocity, respectively
u non-dimensional velocity component in x-direction
v non-dimensional velocity component in y-direction
w non-dimensional velocity component in z-direction
x axial coordinate for the hydrodynamic entrance region
(x, y, z) Cartesian coordinate
x^* thermal entrance length, $x/D_h\ Pe$.

Greek symbols
α thermal diffusivity
δ_{ij} Kronecker delta
φ, ψ interpolation functions
μ coefficient of viscosity
ν coefficient of kinematic viscosity
ρ fluid density.

Subscripts
i, j, k directions of Cartesian coordinate
h hydraulic
m mean
w wall
x derivative w.r.t. x
$,i$ partial derivative w.r.t. i.

Superscripts
$*$ refers to dimensional value
$\sim$ intermediate value.

Nondimensional numbers
Ar aspect ratio, R/a
Nu Nusselt number, hL/k
Pr Prandtl number, ν/α
Re Reynolds number, DU/ν
Pe Peclet number, UD/α
De Dean number, $Re\sqrt{a/R}$.

Note: The symbols defined above are subject to alteration on occasion.

ANALYSIS

Description of the model

The model developed in this study is a part of a square helical duct of small aspect ratio. To obtain the design values of the heat transfer coefficient at the thermal entrance region, models with three aspect ratios were made. The cases analysed were for helical ducts of aspect ratio 3, 6 and 13, where aspect ratio is the ratio of the diameter of the helix to the width of one edge of the duct. Fully developed parabolic velocity profiles were given at the inlet for all the cases analysed and a constant wall temperature boundary condition is imposed along the walls. Figure 1 shows the geometry of the model. The pitch described in this problem is the distance traveled perpendicular to the plane of the helix when it completes one full turn. For a curved pipe of high aspect ratio a new non-

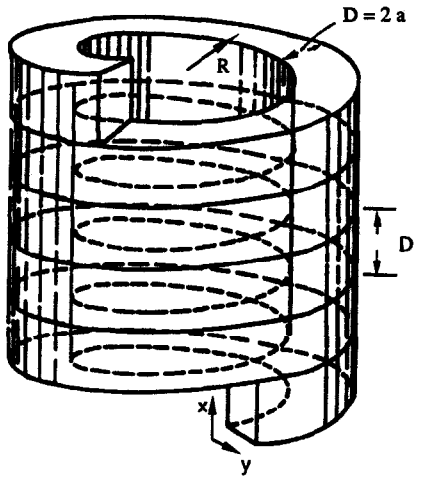

FIG. 1. Geometry of the helical duct.

dimensional parameter can be defined as the Dean number which represents the single non-dimensional number characterizing flow in curved pipe of small pitch and for aspect ratio $Ar \gg 1$. In a helical coil of lower aspect ratio this relation alone cannot describe the flow. In a helical coil, the effective radius of curvature R_c of each turn is influenced by the coil pitch b, and is given by:

$$R_c = R\left[1+\left(\frac{b}{2\pi r}\right)^2\right]. \quad (1)$$

The Nusselt number is defined based on the inlet temperature as the reference, i.e.:

$$Nu_{x,bc} = \frac{h_x D_h}{k} = \frac{q''_x D_h}{k(T_{w,m}-T_0)}. \quad (2)$$

Critical Reynolds number

A transition from laminar to turbulent flow is identified by a critical Reynolds number Re_{crit}. Because of the gradual change in the friction factor in a curved pipe, it is difficult to identify the critical Reynolds number from the friction factor vs Reynolds number curve. Experiments by White [1] confirmed that the flow in a curved pipe is much more stable than that in a straight pipe, so, whereas the critical Reynolds number of the latter is typically around 2000, in a curved tube of even small curvature it may be larger by a factor of two or more. Kakac *et al.* [11] recommended the use of the below correlation for helical pipes:

$$Re_{crit} = 2100\left[1+12\left(\frac{R}{a}\right)^{-0.5}\right], \quad (3)$$

which is derived by Srinivasan *et al.* [12]. This correlation is correct in the limiting case of straight tube $Re_{crit} = 2100$. The cases analysed in this study are in the laminar range.

Governing equations

The problem consists of flow in a helical duct of square cross-section with a heated wall as depicted in Fig. 1 where the fluid enters the domain with a fully developed parabolic velocity profile. The governing equations are the steady three-dimensional Navier–Stokes equations for incompressible flow with constant properties, and the energy equation:

$$(\rho u_j^*)_{,j} = 0, \quad (4)$$

$$\rho(u_j^* u_{i,j}^*) = -p_{,i}^* + \mu u_{i,jj}^*, \quad (5)$$

$$\rho C_p(u_j^* T_{,i}) = (kT_{,i})_{,i}. \quad (6)$$

Boundary conditions and assumptions

A fully developed parabolic velocity profile is given as the inlet velocity boundary condition in all the cases. The integrated value of the velocity at the inlet has a non-dimensionalized value of one. A shear stress free boundary condition is specified at the exit of the duct since the end of the duct is open to the atmosphere. The fluid is incompressible.

No-slip boundary conditions are imposed on all of the solid–liquid interfaces. A non-dimensionalized temperature of unity is imposed on all four walls of the duct starting at a length of $2D$ from the entrance. The effect of gravity is not taken into account. Also, the heat generation due to viscous dissipation is neglected since we are looking at low Reynolds number flows. Since the flow properties are taken to be temperature independent, the buoyancy term in the momentum equation is neglected, i.e. the buoyancy and any temperature dependence in the momentum equation is neglected. This allows us to solve the momentum equations to get a velocity field and use this velocity field to obtain a solution to the energy equation for different Prandtl numbers.

Non-dimensionalization

Dimensionless formulation of problems has many advantages. Scaling the fundamental variables with respect to typical values and constructing dimensionless parameters provide a measure of relative importance of the various terms in the equations and identifies the dominant physical phenomena. It facilitates the performance of parametric studies through the variation of a single parameter.

In this model, the velocity and pressure are scaled as follows: $u = U/W_0$, $v = V/W_0$, $w = W/W_0$, $p = P/\rho W_0$. All the geometric parameters are non-dimensionalized with respect to the duct height D as follows: $x = X/D$, $y = Y/D$, $z = Z/D$, $r = R/D$, $b = B/D$. We introduce the following non-dimensional numbers: $Re = U_0 D/\nu$, $Pr = \mu C_p/k_f$, $Pe = Re\ Pr$.

The temperature is scaled with respect to the inlet temperature by setting $T^* = (T-T_0)/(T_w-T_0)$. By introducing the above non-dimensional parameters, the momentum and energy equations are transformed to:

$$(u_j)_{,j} = 0, \quad (7)$$

$$\rho(u_j u_{i,j}) = -p_{,i} + \frac{1}{Re}u_{i,jj}, \quad (8)$$

$$(u_j T_{,i}^*) = \frac{1}{Re\ Pr}(kT_{,i}^*)_{,i}. \quad (9)$$

To vary the non-dimensional parameters such as the Reynolds number and Prandtl number it is necessary to vary dimensional quantities such as density and velocity. To keep the setting of the characteristic numbers consistent and clear, the inlet velocity, viscosity and conductivity were set to 1. Hence the value of density is set equal to the Reynolds number and specific heat to the Prandtl number.

METHOD OF SOLUTION

The next step in the modeling process is to solve the non-linear partial differential equations governing the

flow. The equations are solved using the finite element code FIDAP [9]. The finite element method (FEM) has some very desirable properties, the most important among them being the capacity to handle irregular geometries. The finite element procedure begins with the division of the continuum region of interest into a number of simply shaped regions called elements. Since the Eulerian description of fluid motion was used in the field equations these elements are assumed to be fixed in space. Within each element the dependent variables u_i, p, T are interpolated by functions of compatible order, in terms of values to be determined at a set of nodal points. The partial differential equation for a three-dimensional steady-state problem within each element is replaced by:

Momentum: $[f_1(\varphi, \psi, \vartheta, u_i, p, T) = R_1]$

Incompressibility: $[f_2(\varphi, u_i,) = R_2]$

Energy: $[f_3(\varphi, \vartheta, u_i, T) = R_3]$

where u_i, p and T are the column vectors of element nodal point unknowns. The symbols R_1, R_2, R_3 represent the residual errors due to the above approximation. With the aid of optimization methods these residuals are minimized by establishing orthogonality between the residual matrix and the interpolation matrix.

In FIDAP [9] there are two solution procedures. The first approach solves all conservation equations in a simultaneous coupled manner, while the second approach solves each equation separately in a sequential manner (segregated approach). In this problem a segregated approach is utilized to obtain a solution to the velocity field since the size of the model restricts the use of a fully coupled solver. The temperature field is solved by using a quasi-Newton method.

Spatial discretization in the finite element method involves dividing the physical domain into small elements which could be of any shape such as a brick or tetrahedron. The unknown function is assumed to have a polynomial variation within the element and is expressed in terms of the nodal variables. Depending on the type of polynomial variation desired we need to place that many nodes in each element. In this model, 8 node linear brick elements were selected. With this spatial discretization and the use of the Galerkin finite element formulation, we arrive at a system of matrix equations.

For unusually large two-dimensional problems and three-dimensional problems the peripheral storage required for the global system matrix can become excessive. In this approach the matrix equations arising from the FEM discretization of the flow equations is solved in a sequential manner for velocity, temperature and pressure. The most important difference between a coupled solver is that it avoids the direct formation of a global system matrix. Instead, this matrix is decomposed into smaller submatrices each governing the nodal unknowns associated with only one conservation equation. These smaller submatrices are then solved sequentially using conjugate gradient type schemes. As the storage required for the individual submatrices is less than that needed to store the global system matrix, the storage requirements of the segregated approach are substantially less than that of the fully coupled approach. The following section from ref. [9] details the structure of the segregated algorithm.

Structure of the segregated algorithm

The equation:

$$\mathbf{K}(\mathbf{u})\mathbf{u} = \mathbf{F}, \tag{10}$$

represents the global discretized matrix problem resulting from the application of the Galerkin FEM to the fluid flow equations. The global vector of unknowns U will have the composition $U = (\mathbf{u}, p, T)$ where $\mathbf{u}$ is the vector of velocity components, $\mathbf{u} = (u, v, w)$. In the segregated algorithm equation (10) is never formed directly. It is decomposed into the following set of decoupled sub-matrix systems for the continuity, the temperature and the momentum equations:

$$\mathbf{K}_u u - \mathbf{C}_x p = \mathbf{f}_u \quad \mathbf{K}_v v - \mathbf{C}_y p = \mathbf{f}_v \quad \mathbf{K}_w w - \mathbf{C}_z p = \mathbf{f}_w \tag{11}$$

$$\mathbf{C}_x^{\mathrm{T}} u + \mathbf{C}_y^{\mathrm{T}} v + \mathbf{C}_z^{\mathrm{T}} w = 0 \quad \mathbf{K}_{\mathrm{T}} T = \mathbf{f}_{\mathrm{T}}. \tag{12}$$

In the above equations, the $\mathbf{K}_u$, $\mathbf{K}_v$ and $\mathbf{K}_w$ matrices incorporate the combined effects of advection and diffusion. The $\mathbf{C}_x$, $\mathbf{C}_y$ and $\mathbf{C}_z$ matrices and their transposes are the pressure gradient and velocity divergence operators, respectively. The right hand side $\mathbf{f}_u$, $\mathbf{f}_v$, $\mathbf{f}_w$ and $\mathbf{f}_{\mathrm{T}}$ vectors represent the combined effects of gradient type boundary conditions.

The above system of matrix equations is not yet amenable to a segregated approach as an explicit matrix equation for pressure does not appear in these equations. Such an equation can be obtained by replacing the continuity equation, which implicitly governs the level of pressure, with a Poisson type pressure matrix equation. This is done by algebraic manipulations of the above discretized momentum and continuity equations, which forces the satisfaction of the discretized continuity equation. The pressure projection approach used in this solution procedure comprises three main steps. At the beginning of an iteration, an approximation to the pressure is obtained from the solution of a Poisson type pressure matrix using the latest available values of the field variables. The various components of the momentum equations and any other conservation equations present in the flow problem are then solved using the most recent field variables. Finally, at the end of the iteration the velocity field is mass-adjusted via an irrotational projection onto a divergence free sub-space. This last step involves the solution of another Poisson type matrix equation for a pressure correction vector ΔP.

Given an initial solution field (u^0, v^0, w^0, T^0) for

$i = 0, 1, 2, \ldots$ until convergence proceed as follows:

(1) Evaluate Poisson matrix equation for pressure:

$$[\mathbf{C}_x^{\mathrm{T}}(\tilde{\mathbf{K}}_u^{-1})^*\mathbf{C}_x + \mathbf{C}_y^{\mathrm{T}}(\tilde{\mathbf{K}}_v^{-1})^*\mathbf{C}_y]p_{i+1/2} = -\mathbf{C}_x^{\mathrm{T}}(\tilde{\mathbf{K}}_u^{-1})^*[\mathbf{f}_x^* - (\tilde{\mathbf{K}}_u)^*u_i] - \mathbf{C}_y^{\mathrm{T}}(\tilde{\mathbf{K}}_v^{-1})^*[\mathbf{f}_y^* - (\tilde{\mathbf{K}}_v)^*v_i]. \quad (13)$$

(2) Relax the pressure:

$$p^{i+1} = \alpha_p^i + (1-\alpha_p)p^{i+1/2}. \quad (14)$$

(3) Evaluate x-momentum equation for u:

$$\left[\left(\frac{\alpha_u}{1-\alpha_u}\right)\tilde{\mathbf{K}}_u + \mathbf{K}_u\right]^* u^{i+1/2} = \mathbf{f}_x^* + \mathbf{C}_x p^{i+1} + \left(\frac{\alpha_u}{1-\alpha_u}\right)\tilde{\mathbf{K}}_u^*\mathbf{u}^i. \quad (15)$$

(4) Evaluate y-momentum equation for v:

$$\left[\left(\frac{\alpha_v}{1-\alpha_v}\right)\tilde{\mathbf{K}}_v + \mathbf{K}_v\right]^* v^{i+1/2} = \mathbf{f}_y^* + \mathbf{C}_y p^{i+1} + \left(\frac{\alpha_v}{1-\alpha_v}\right)\tilde{\mathbf{K}}_v^*\mathbf{v}^i. \quad (16)$$

(5) Evaluate the z-momentum equation for w:

$$\left[\left(\frac{\alpha_w}{1-\alpha_w}\right)\tilde{\mathbf{K}}_w + \mathbf{K}_w\right]^* w^{i+1/2} = \mathbf{f}_z^* + \mathbf{C}_z p^{i+1} + \left(\frac{\alpha_w}{1-\alpha_w}\right)\tilde{\mathbf{K}}_w^* w_i. \quad (17)$$

(6) Evaluate the Poisson matrix for ΔP

$$[\mathbf{C}_x^{\mathrm{T}}(\tilde{\mathbf{K}}_u^{-1})^*\mathbf{C}_x + \mathbf{C}_y^{\mathrm{T}}(\tilde{\mathbf{K}}_v^{-1})^*\mathbf{C}_y + \mathbf{C}_z^{\mathrm{T}}(\tilde{\mathbf{K}}_w^{-1})^*\mathbf{C}_z]\Delta P = -\mathbf{C}_x^{\mathrm{T}}u^{i+1/2} - \mathbf{C}_y^{\mathrm{T}}v^{i+1/2} - \mathbf{C}_z^{\mathrm{T}}w^{i+1/2}. \quad (18)$$

(7) Adjust velocity field:

$$u^{i+1} = u^{i+1/2} + (\tilde{\mathbf{K}}_u^{-1})^*\mathbf{C}_x\Delta P, \quad (19)$$

$$v^{i+1} = v^{i+1/2} + (\tilde{\mathbf{K}}_v^{-1})^*\mathbf{C}_y\Delta P, \quad (20)$$

$$w^{i+1} = w^{i+1/2} + (\tilde{\mathbf{K}}_w^{-1})^*\mathbf{C}_z\Delta P. \quad (21)$$

In the above equations the superscripts i, $i+1/2$ and $i+1$ denote previous, intermediate and latest iteration levels, respectively. The superscript * denotes the latest available field variable. The $\tilde{\mathbf{K}}$ matrices appearing in the above equations are convenient approximations to their corresponding $\mathbf{K}$ matrices. These are used both in the construction of the Poisson type matrices, and on the either side of the conservation equations to affect the relaxation of these equations. The $\tilde{\mathbf{K}}$ matrices are diagonal matrices obtained from the following expressions:

$$(\tilde{\mathbf{K}}_u)_{ii} = \sum_j |(\mathbf{K}_u)_{ij}| \quad (\tilde{\mathbf{K}}_v)_{ii} = \sum_j |(\mathbf{K}_v)_{ij}| \quad (\tilde{\mathbf{K}}_w)_{ii} = \sum_j |(\mathbf{K}_w)_{ij}|. \quad (22)$$

The αs appearing in equations (14)–(17) are relaxation factors which assume values between 0 and 1. After solving the momentum equations, the velocity field is used to obtain the temperature field solution using the quasi-Newton algorithm. Our problem model has 481 nodes in the cross-sectional plane which are non-uniformly distributed. The axial distance between the elements is progressively increased as we go along the length since the gradients in the solution variables in that direction decreases with increase in axial length. An optimum value for the αs in the segregated approach is arrived by a numerical experiment in order to arrive at value which reduces the oscillation in the solution variables. We chose the same α for all the components of velocity. Very tight convergence criteria are imposed for the symmetric matrix iteration in the segregated algorithm, since the solution from this is used in the non-symmetric matrix iteration. The velocity solutions took approximately 1 h of CPU time on a CRAY Y-MP for each run and the solution of the energy equation took approximately 160 s of CPU time on a CRAY-2.

RESULTS AND DISCUSSION

To verify the numerical model, a flow through a straight three-dimensional square duct is simulated. The heat transfer boundary conditions were imposed at a length of $2D$ from the entrance to ensure that the flow is fully developed when it encounters the heated walls, i.e. in the region where the temperature boundary condition exists the hydrodynamic boundaries completely fill the duct cross-section and the velocity profile is of an invariant form $w = w(x, y)$, $u = v = 0$.

The flow field is solved using the segregated solution approach detailed earlier. Convergence is declared when the relative change in the solution variables between two successive iterations is found to be less than 0.001, i.e. $\|\mathbf{u}_i - \mathbf{u}_i - 1\|/\|\mathbf{u}_i\| \leqslant 0.001$, where the vector $\mathbf{u}$ comprises all the nodal values of a particular degree of freedom. The norm $\|\cdot\|$ is a root mean squared norm summed over all the equations for the model. At steady state the discharge at every cross-section (Q_x) must be equal to the inlet discharge (Q), or in other words $\mathrm{d}Q_x/\mathrm{d}x = 0$. This is a good check to verify if mass is being conserved. The error in the conservation of mass is found to be less than 1%. The flow field obtained in this case is used as the initial solution to solve the energy equation. This approach is possible since the fluid properties are taken to be temperature independent.

Constant wall temperature boundary condition

The temperature field for the three Prandtl numbers of 0.7, 3.0 and 7.01 is obtained by solving the energy equation using the velocity field obtained from the solution of the isothermal flow through the square duct. These Prandtl numbers were selected since they represent the fluids which have properties between that of air and water. The solution is obtained for

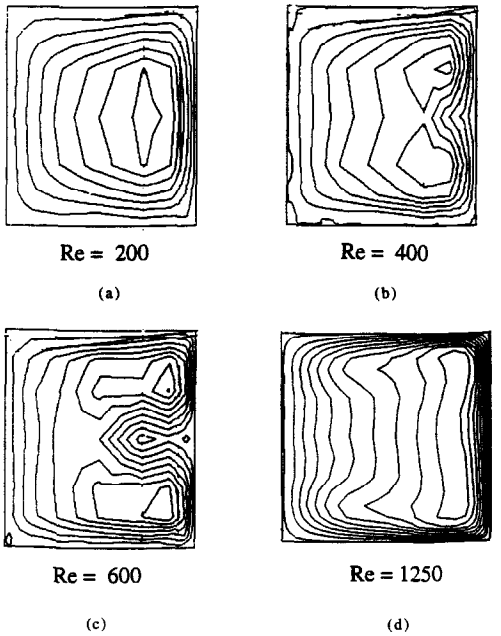

FIG. 2. Fully developed axial velocity contours: $Ar = 13$, $L = 9D$.

forced convection by setting $Gr = 0$ (no free convection) and solving the energy equation. The computer code is tested for a Prandtl number of 0.7. The local Nusselt number for the hydrodynamically fully developed and thermally developing flow compared well with that of Chandrapatla and Shasthri [10]. The Nusselt number is defined as $Nu_{x^*,T} = h_x D/k = q'' D/(k(T_{w,m} - T_m))$, where T_m is the fluid bulk mean temperature defined by $T_m = 1/A_c u \int_{A_c} uT \, dA_c$. The solution is repeated for a lower mesh density of 15×15 and no noticeable change in Nusselt number is observed. After gaining confidence in the model, results were obtained for Prandtl numbers 3 and 7.01.

Developing flow in helical ducts

It is known that the flow through a helical duct is characterized by a secondary flow field caused by the unbalanced centrifugal forces in the curved duct. Secondary flow produces a transport of the fluid over the cross-section of the duct, causing the axial velocity profile to be slanted toward the outside of the coil. The fluid is forced outward, creating higher pressure to balance the momentum caused by the secondary flow. The secondary flow transports the fluid from the inner wall to the outer wall, and the boundary layer near the inner wall develops much faster than in a straight duct.

From the axial velocity contours (Fig. 2), it can be observed that the axial velocity is influenced by the secondary flow. The development of the boundary layer near the outer wall is slower compared to the boundary layer near the inner wall. Hence the momentum boundary layer thickness on the outer wall is much smaller than that on the inner wall. Thus, when you compare the axial velocity profiles with that of a straight duct, the velocity contours in a straight duct are compressed toward the outer wall in a helically coiled duct.

To understand the development of flow with increasing Dean numbers, solutions were obtained for Reynolds numbers ranging from 50 to 1750 for a helical duct of aspect ratio 13 and pitch $1.68D$. Figure 2a–d shows the fully developed axial velocity contours at a cross-section $9D$ from the entrance for a Reynolds number of 200, 400, 600 and 1250. It can be noticed that in Fig. 2a the contours of maximum axial velocity are shifted towards the outer wall. As the Reynolds number is increased to 400 the centrifugal force, which is proportional to the velocity, increases. This high centrifugal force creates a region of high pressure at the middle of the outer wall which reduces the axial velocity at that region.

At a higher Reynolds numbers of 600 Fig. 2c indicates the formation of an additional vortex at the high pressure region. The reason for this phenomena is that the contour lines of axial velocity are densely distributed near the outer wall and the pressure is raised due to centrifugal force proportional to ω^2 acting in that region, ω being the radial velocity. At a certain Reynolds number stagnation appear in the central part of the outer wall due to the existence of a high pressure region where the large centrifugal force is acting. This causes the formation of an additional vortex. The strength of this additional vortex increases from a Reynolds number of 600 to 700. The contour lines of axial velocity show that the position of maximum axial velocity at which the centrifugal forces become maximum, exists on the boundary line between the secondary and additional vortices. The two high velocity regions at this Reynolds number exist at regions between the top and bottom walls and the additional vortex. Thus the centrifugal forces acting on the axial flow cause the secondary and additional vortex flows. The additional vortex flows inward along the radial line as the Reynolds number increases. This additional vortex disappears when the Reynolds number is increased further. Figure 2d shows the fully developed axial velocity contour at a Reynolds number of 1250, which shows that the additional vortex has disappeared. The reason for this disappearance could be explained as follows. This additional vortices causes a reduction in the axial velocity at the central outer region of the duct. The reduction in the axial velocity causes a reduction in the centrifugal forces acting on the fluid elements on the region which in turn causes a reduction in the pressure due to centrifugal force. Thus, when the Reynolds number increases additional vortices are swept away and the secondary flow is restabilized to a double vortex configuration. Thus the centrifugal force at a certain Reynolds number range affects the appearance, disappearance and reappearance of the additional vortices. The Reynolds number range

within which this happens depends on the aspect ratio of the duct, the duct geometry and the inlet velocity profile.

Figure 3 shows the axial velocity contours at three cross-sections along the length in the helical duct of aspect ratio 3. At the entrance we have an imposed fully developed parabolic velocity profile. At 180° the axial velocity profile is still developing and an additional vortex can be observed at a region below the center line. This may be attributed to the unbalanced secondary force due to the effect of pitch. However, this additional vortex disappears as the flow becomes fully developed. This can be noticed from the axial velocity contours at the 360° plane. It is known that in the case of a curved duct without pitch, the two secondary flow vortices formed are symmetric to each other. Based on this, the axial velocity is also symmetric to a line drawn at the center of the duct. But in the case of a helical duct, the symmetric shape is distorted due to the effect of pitch. At the fully developed section it can be seen (Fig. 3) that the axial velocity contours shift slightly toward the top right corner. This confirms the results of Kumar *et al.* [5]. A crescent moon like shape is observed for the fully developed axial velocity contours.

Heat transfer in helical ducts

As the first fluid enters the helical duct the secondary flow causes a change in temperature between the outer and inner wall. During this interval the thermal boundary layer merely transmits most of the heat, and the temperature in the thermal boundary layer does not increase substantially because heat is convected away from its outer edge. When the heat carried by the secondary flow encounters the thermal boundary layer on the outer wall, the temperature at the outer edge of the thermal boundary layer is suddenly increased. Here the Nusselt number drops suddenly and temperature rises rapidly. This interaction between secondary flow and heat transfer accounts for the first cycle in the oscillations.

Near the tube inlet and at a low Dean number the development of the temperature field is similar to that in a straight duct. The thermal boundary layer is thin and its penetration into the secondary flow field is insufficient for the effect of the secondary flow to be significant. However, the secondary flow velocities increase rapidly with increasing axial distance, and the thermal boundary layer grows with advancing axial distance. The growth of the thermal boundary layer is suppressed, and the secondary convection transfers most of the heat into the fluid core. This phenomena causes a cyclic variation of heat transfer, temperature and local Nusselt number along the axial length until the temperature field is fully developed. Since the relative rate of heat transport by secondary convection, compared with axial convection, increases with increase in Reynolds and Prandtl number, the intensity of the cyclic behavior must increase with increasing Reynolds number and Prandtl number. This can be observed in Fig. 4.

One consequence of the phenomena of cyclically varying wall temperature is a cyclically varying local Nusselt number based on the difference between the wall and bulk temperature. The cyclic variation damps out as a fully developed temperature profile is approached and the Nusselt number approaches an asymptotic value. The oscillation arises because of the fact that at the thermal entrance region, even at high aspect ratios, the fluid core is not well mixed. As a result the convective propagation of a temperature change through the core involves definite time delays.

Figure 4 shows the periphery averaged local Nusselt number for aspect ratios of 3, 6 and infinity (∞) for

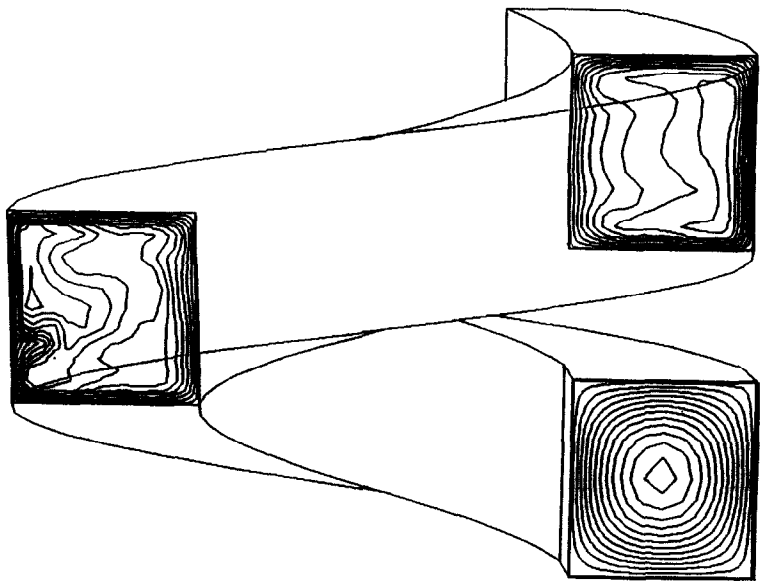

FIG. 3. Axial velocity contours at three cross-sections: $Ar = 3$, $Re = 500$, $Pr = 0.7$, $\phi = 0°$, 180° ad 360°.

a Reynolds number of 750. As compared to straight ducts, helical ducts are compact and yield higher heat transfer coefficients. At the outer wall of the duct the higher velocities reduce the thermal resistance considerably resulting in high heat transfer coefficients. The Nusselt number and hence the heat transfer in helical ducts increase with increase in aspect ratio. The variation becomes lower as the aspect ratio becomes smaller. At a Prandtl number of 0.7, the difference between the Nusselt numbers for the helical ducts of aspect ratios 3 and 6 is not substantial, but it can be observed that helical ducts have a higher heat transfer rate compared to the straight duct. As the Prandtl number is increased to 3.0, the increase in heat transfer with that of a straight duct increases. The heat transfer increases further as the Prandtl number is raised to 7.01. At a higher Prandtl number the heat carried by the secondary flow increases which causes more cyclic variation of the wall temperature and Nusselt number. A steady decline in the Nusselt number can be observed for the case of aspect ratio ∞ as expected. Figure 5 presents the local Nusselt numbers for a Reynolds number of 500 for the three aspect ratios 3, 6, 13 and ∞. Similar trends in the variation of Nusselt number can be observed. Figure 6 shows the variation of local Nusselt number with Reynolds number for a helical duct of aspect ratio 13 and for a Prandtl number of 0.7.

We now present the variation of local Nusselt number along the periphery at four cross-sections to discuss the variation of Nusselt number between the edges. The results presented are for a Reynolds number of 500 and Prandtl number of 0.7 which form only a fraction of the data which could be presented. The temperature contour plots and the local Nusselt number plots are shown to give a physical interpretation of the development of temperature field. For a Prandtl number of 0.7 the temperature profiles are similar to

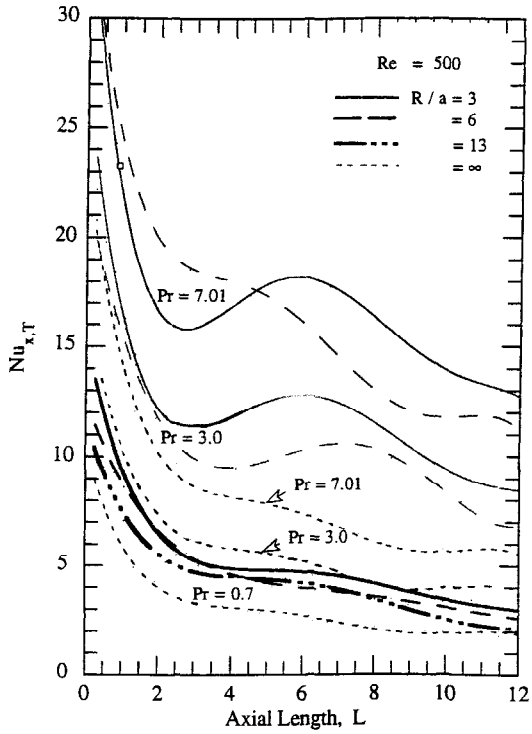

FIG. 5. Local Nusselt number at the thermal entrance region: $Re = 500$, $R/a = 3$, 6, 13 and infinity.

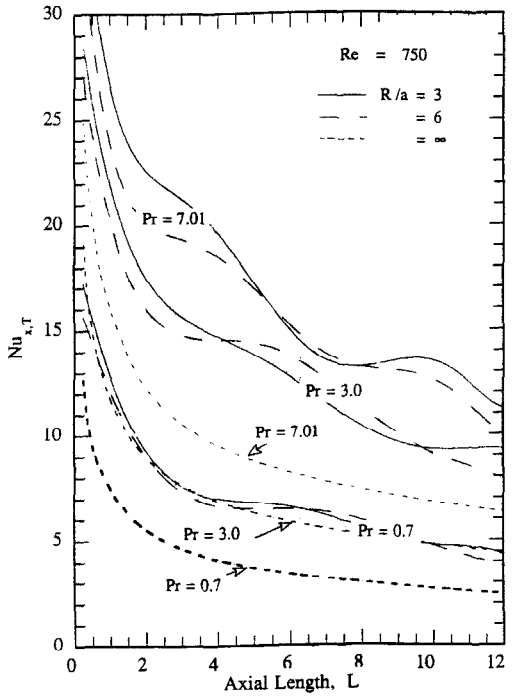

FIG. 4. Local Nusselt number at the thermal entrance region: $Re = 750$, $R/a = 3$, 6 and infinity.

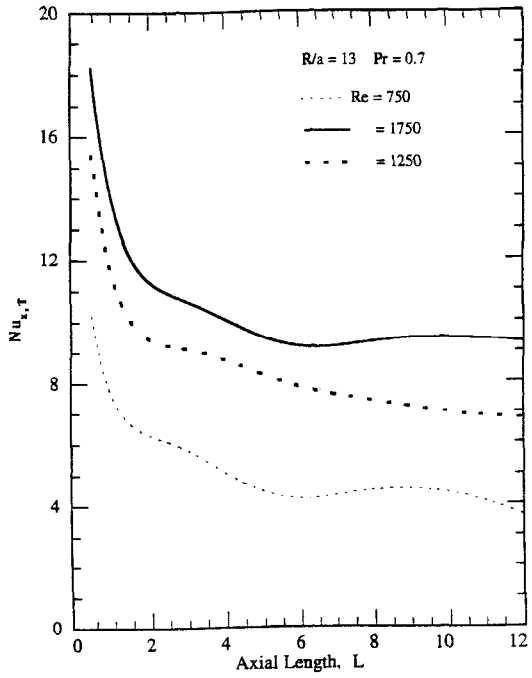

FIG. 6. Local Nusselt number at the thermal entrance region: $R/a = 13$, $Pr = 0.7$, $Re = 750$, 1250 and 1750.

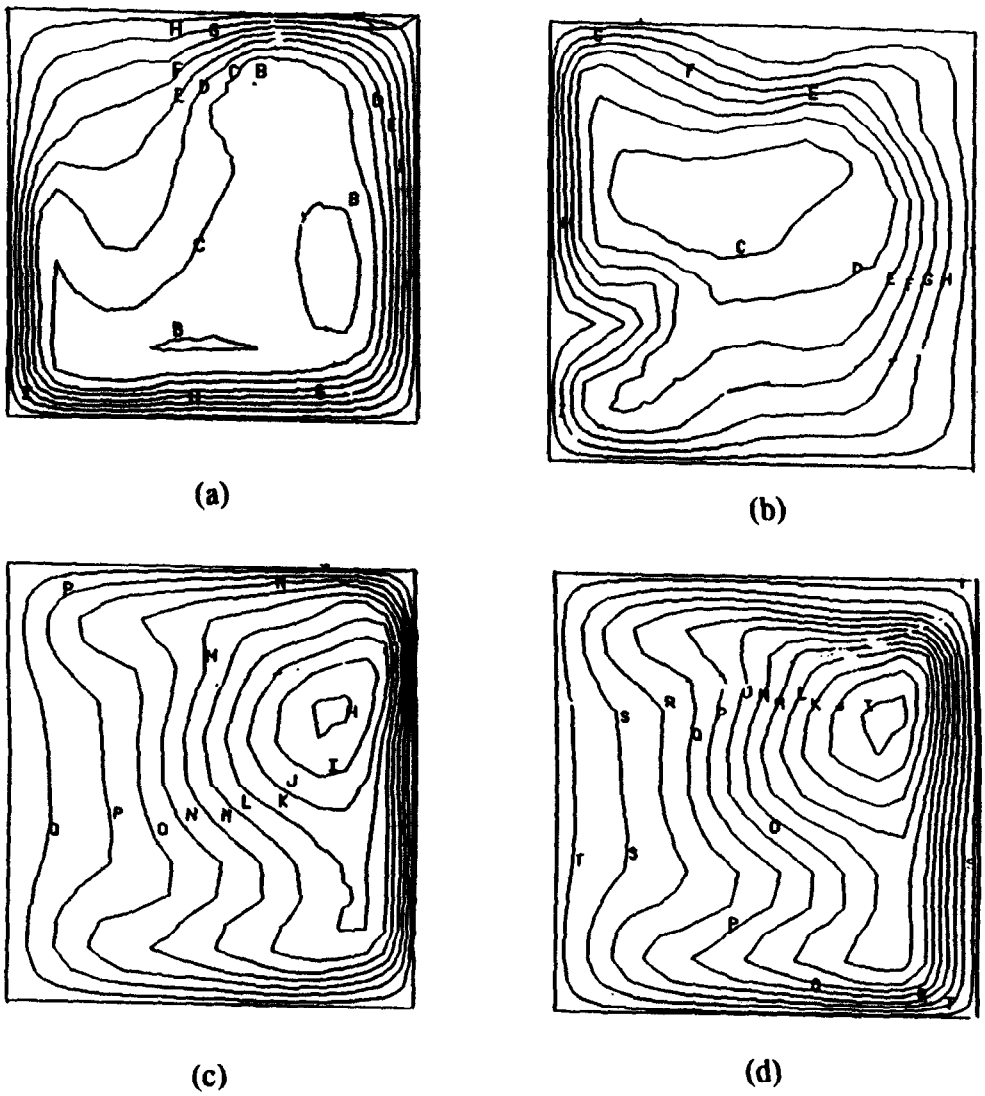

FIG. 7. Temperature contours at four cross-sections: $L = 2.35D$, $4.71D$, $9.42D$ and $11.0D$.

the velocity profiles since the momentum and temperature profiles develop at the same rate. Figures 7(a) and 8 show the temperature contours and local variation of Nusselt number along the periphery at an axial distance of $2.35D$ from the entrance. The temperature contours indicate that the temperature field is not fully developed. At this section the variation of heat transfer coefficient between the four edges is not substantial. But the peak values are shifted off the center because of the presence of flow in the cross-sectional plane. The inner bottom corner area has the lowest value of Nusselt number.

As we go further downstream the variation of Nusselt number between the four walls increases. Figures 7(b) and 8 show the local Nusselt number plot at an axial length of $4.71D$ from the entrance. At the outer edge, starting from the bottom point, an increase in heat transfer coefficient can be noticed until a point below the center line. At that point the Nusselt number drops sharply because of the presence of an additional vortex which reduces the axial velocity at that region. The Nusselt number again climbs to reach a maximum value at a point between the mid line and the top corner. It can also be noticed that the Nusselt number at the corner points does not become zero as in the case of a straight square duct. On the top edge the Nusselt number again climbs to a peak at a point located closer to the outer edge and then drops gradually to reach the minimum value at the corner. On the inner edge, the variation is similar to that on a square duct except for a sudden climb as it approaches the center. This is because of the presence of incoming secondary flow from the top and bottom corners. At the bottom wall, a steady increase of the Nusselt number is observed from the inner corner to the outer corner. The peak is seen at a region beyond half distance from the corner since the axial velocity is shifted towards the outer edge of the helical duct. Similar trends are observed at a length of $9.42D$ and $11D$ from the entrance as can be seen in Figs. 7(c) and (d), and

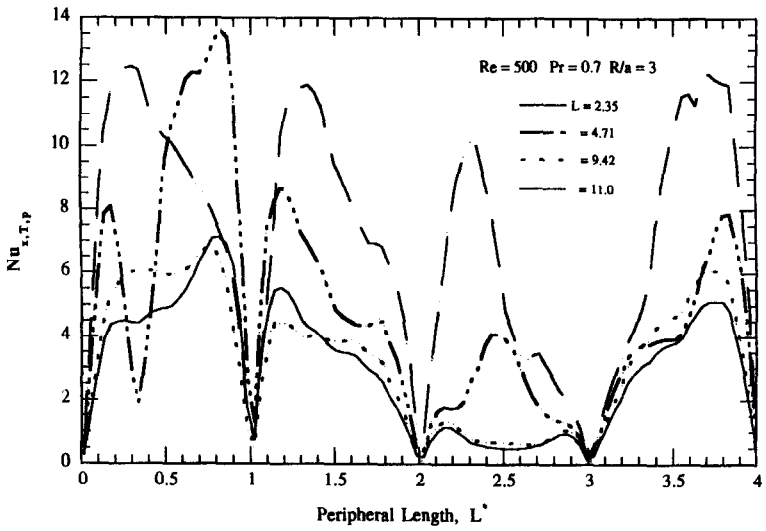

FIG. 8. Variation of Nusselt number along the periphery of the duct: $Re = 500$, $Pr = 0.7$, $R/a = 3$.

8. It can be observed that there is a relative increase in heat transfer at the corners compared to the previous plots which indicate that the secondary flow is a dominant phenomena as the flow become fully developed.

Figure 9 shows the peripheral Nusselt number at a length of $11.7D$ for the square duct, and helical ducts of aspect ratios 3 and 6. For the square duct the variation is similar on all the four edges. It can be noticed that the Nusselt numbers on the outer, top and inner edges are substantially higher than that of a square duct which explains the increase in heat transfer rates in a helical duct. Also, it can be noticed that the difference in heat transfer between the two helical ducts is less compared to the difference with a straight duct. This indicates that, at very low aspect ratios, variation in Ar does not substantially improve the heat transfer.

We have investigated the physical reasons for the peripheral variation of Nusselt number in helicoidal ducts. The effect of the Prandtl number on temperature profiles is analysed. The heat convected by the secondary flow increases with the increase in Prandtl number. The model predicts that the percentage increase in heat transfer, with the increase in Prandtl number, decreases as the aspect ratio becomes small. The peripheral variation of local Nusselt number shows that the heat transfer coefficient on the outer wall is substantially higher than that on the inner edge, which confirms the known result. It is shown in the analysis that the flow field can be predicted by analysing the peripheral variation of local

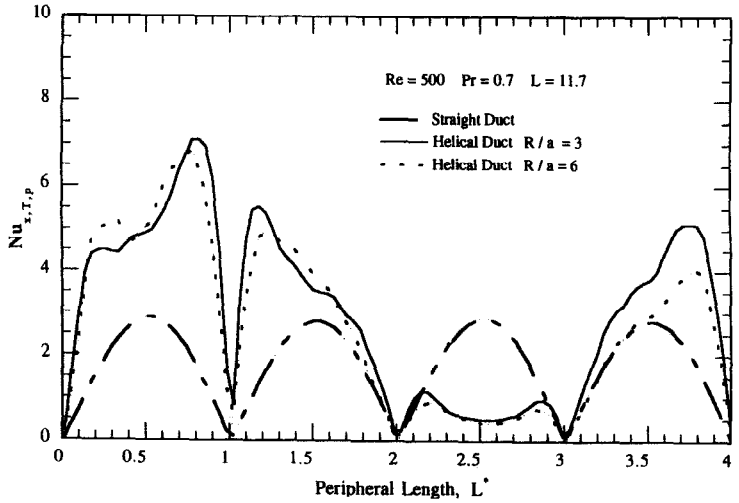

FIG. 9. Nusselt number along the periphery at a length of $11.7D$ from the entrance: $Re = 500$, $Pr = 0.7$, $L = 11.7D$.

Nusselt number. The comparison of the numerical results with the known exact values for the limiting case of the straight duct shows excellent agreement.

Acknowledgement—This paper is based upon work supported by Texas Advanced Technology Program under grant # 003604-027.

REFERENCES

1. C. M. White, Streamline flow through curved pipes, *Proc. R. Soc. London, Sec. A* **123,** 645–663 (1929).
2. E. Largaespada, I. Muguercia, W. Li and M. A. Ebadian, An experimental investigation of fluid flow inside a helicoidal pipe, *FED Contributed Papers Fluids Engng* **139,** 9 (1992).
3. Chia-Fu Hsu and S. V. Patankar, Study of laminar non-Newtonian flow and heat transfer in curved tubes, *A.I.Ch.E. J.* **28,** 610 (1982).
4. Y. Mori, Y. Uchida and T. Ukon, Forced convective heat transfer in a curved channel with a square cross section, *Int. J. Heat Mass Transfer* **14,** 1787–1805 (1971).
5. K. R. Kumar, Fully developed flow of power law fluids in curved ducts with heat transfer, *Numer. Heat Transfer A* **16,** 101 (1989).
6. B. Joseph, E. P. Smith and R. J. Adler, Numerical treatment of laminar flow in helically coiled tubes of square cross section, Part I. Stationary helically coiled tubes, *A.I.Ch.E. J.* **21,** 965 (1975).
7. K. C. Cheng and M. Akiyama, Laminar forced convection heat transfer in curved rectangular channels, *Int. J. Heat Mass Transfer* **13,** 471–490 (1970).
8. K. N. Ghia and J. S. Sokhey, Laminar incompressible viscous flow in curved rectangular channels, *J. Fluid Engng* **99,** 640–648 (1977).
9. M. Engleman, *FIDAP Theoretical Manual* (version 6). Fluid Dynamics International, 500 Davis St., Suite 600, Evanston, IL 60201 (1992).
10. A. R. Chandrupatla and V. M. K. Sastri, Laminar forced convection heat transfer of a non-Newtonian fluid in a square duct, *Int. J. Heat Mass Transfer* **20,** 1315–1324 (1977).
11. S. Kakac, R. K. Shah and W. Aung, *Handbook of Single-phase Convective Heat Transfer*. John Wiley (1987).
12. P. S. Srinivas, S. S. Nandapurkar and F. A. Holland, Friction factors for coils, *Trans. Instn Chem. Engrs* **48,** T156–T161 (1970).